## **OPEN ACCESS**



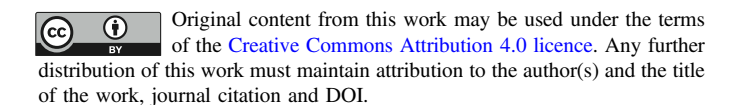
# SN 2023ixf in Messier 101: Photo-ionization of Dense, Close-in Circumstellar Material in a Nearby Type II Supernova

```
W. V. Jacobson-Galán<sup>1,30</sup>, L. Dessart<sup>2</sup>, R. Margutti<sup>1,3</sup>, R. Chornock<sup>1</sup>, R. J. Foley<sup>4</sup>, C. D. Kilpatrick<sup>5</sup>, D. O. Jones<sup>6</sup>
K. Taggart , C. R. Angus , S. Bhattacharjee , L. A. Braff , D. Brethauer , A. J. Burgasser , F. Cao , C. M. Carlile , K. C. Chambers , D. A. Coulter , D. A. Coulter , C. B. Dickinson , T. de Boer , A. Gagliano , A. Gagliano , A. Gagliano ,
 C. Gall<sup>7</sup>, H. Gao<sup>12</sup>, E. L. Gates<sup>15</sup>, S. Gomez<sup>16</sup>, M. Guolo<sup>17</sup>, M. R. J. Halford<sup>18</sup>, J. Hjorth<sup>7</sup>, M. E. Huber<sup>12</sup>, M. N. Johnson<sup>19</sup>, P. R. Karpoor<sup>11</sup>, T. Laskar<sup>20</sup>, N. LeBaron<sup>1</sup>, Z. Li<sup>21</sup>, Y. Lin<sup>22</sup>, S. D. Loch<sup>18</sup>, P. D. Lynam<sup>15</sup>, E. A. Magnier<sup>12</sup>, P. Maloney<sup>4</sup>, D. J. Matthews<sup>1</sup>, M. McDonald<sup>22</sup>, H.-Y. Miao<sup>8</sup>, D. Milisavljevic<sup>23</sup>, Y.-C. Pan<sup>8</sup>, S. Pradyumna<sup>22</sup>, C. L. Ransome<sup>24</sup>, J. M. Rees<sup>15</sup>, A. Rest<sup>16,17</sup>, C. Rojas-Bravo<sup>4</sup>, N. R. Sandford<sup>1</sup>,
L. Sandoval Ascencio<sup>25</sup>, S. Sanjaripour<sup>22</sup>, A. Savino<sup>1</sup>, H. Sears<sup>5</sup>, N. Sharei<sup>22</sup>, S. J. Smartt<sup>26,27</sup>, E. R. Softich<sup>11</sup>, C. A. Theissen<sup>11</sup>, S. Tinyanont<sup>4</sup>, H. Tohfa<sup>22</sup>, V. A. Villar<sup>24,28,29</sup>, Q. Wang<sup>17</sup>, R. J. Wainscoat<sup>12</sup>, A. L. Westerling<sup>4</sup>, E. Wiston<sup>1</sup>, M. A. Wozniak<sup>22</sup>, S. K. Yadavalli<sup>24</sup>, and Y. Zenati<sup>17,31</sup>, A. L. Westerling<sup>4</sup>, Department of Astronomy, University of California, Berkeley, CA 94720, USA; wynnjg@berkeley.edu
                                 <sup>2</sup> Institut d'Astrophysique de Paris, CNRS-Sorbonne Université, 98 bis boulevard Arago, F-75014 Paris, France
                                                         Department of Physics, University of California, Berkeley, CA 94720, USA
                                        <sup>4</sup> Department of Astronomy and Astrophysics, University of California, Santa Cruz, CA 95064, USA
<sup>5</sup> Center for Interdisciplinary Exploration and Research in Astrophysics (CIERA), and Department of Physics and Astronomy, Northwestern University, Evanston, IL
                                                                                                  60208, USA
                                                  <sup>6</sup> Gemini Observatory, NSF's NOIRLab, 670 N. A'ohoku Place, Hilo, HI 96720, USA
                                      <sup>7</sup> DARK, Niels Bohr Institute, University of Copenhagen, Jagtvej 128, DK-2200 Copenhagen, Denmark
                             <sup>8</sup> Graduate Institute of Astronomy, National Central University, 300 Zhongda Road, Zhongli, Taoyuan 32001, Taiwan
                                                   Department of Astronomy & Astrophysics, UC San Diego, La Jolla, CA 92093, USA
                                                         Department of Statistics, University of California, Riverside, CA 92521, USA
                                  11 Center for Astrophysics and Space Sciences, University of California, San Diego, La Jolla, CA 92093, USA
                                            Institute for Astronomy, University of Hawaii, 2680 Woodlawn Drive, Honolulu, HI 96822, USA
                                  Department of Astronomy, University of Illinois at Urbana-Champaign, 1002 W. Green St., IL 61801, USA
                                 <sup>14</sup> Center for Astrophysical Surveys, National Center for Supercomputing Applications, Urbana, IL, 61801, USA
                                               University of California Observatories/Lick Observatory, Mount Hamilton, CA 95140, USA
                                                                  Space Telescope Science Institute, Baltimore, MD 21218, USA
                                       <sup>17</sup> Department of Physics and Astronomy, The Johns Hopkins University, Baltimore, MD 21218, USA
                                                 Department of Physics, Auburn University, 380 Duncan Drive, Auburn, AL 36849, USA
                                                         Department of Physics, University of California, Santa Cruz, CA 95064, USA
                                             Department of Physics & Astronomy, University of Utah, Salt Lake City, UT 84112, USA
                                         <sup>21</sup> Department of Earth and Planetary Sciences, University of California, Riverside, CA 92521, USA
                             <sup>22</sup> Department of Physics & Astronomy, University of California Riverside, 900 University Ave, Riverside, CA, USA
                           <sup>23</sup> Department of Physics and Astronomy, Purdue University, 525 Northwestern Avenue, West Lafayette, IN 47907, USA
                 <sup>24</sup> Department of Astronomy and Astrophysics, Pennsylvania State University, 525 Davey Laboratory, University Park, PA 16802, USA
                                         Department of Physics and Astronomy, University of California, Irvine, California 92697-4575, USA
                          Astrophysics Research Centre, School of Mathematics and Physics, Queen's University Belfast, Belfast BT7 1NN, UK
                                                             Department of Physics, University of Oxford, Keble Road, Oxford, UK
                                  <sup>28</sup> Institute for Computational & Data Sciences, The Pennsylvania State University, University Park, PA, USA
                                <sup>29</sup> Institute for Gravitation and the Cosmos, The Pennsylvania State University, University Park, PA 16802, USA
                                      Received 2023 June 7; revised 2023 August 21; accepted 2023 August 21; published 2023 September 8
```

#### **Abstract**

We present UV and/or optical observations and models of SN 2023ixf, a type II supernova (SN) located in Messier 101 at 6.9 Mpc. Early time (flash) spectroscopy of SN 2023ixf, obtained primarily at Lick Observatory, reveals emission lines of H I, He I/II, C IV, and N III/IV/V with a narrow core and broad, symmetric wings arising from the photoionization of dense, close-in circumstellar material (CSM) located around the progenitor star prior to shock breakout. These electron-scattering broadened line profiles persist for  $\sim$ 8 days with respect to first light, at which time Doppler broadened the features from the fastest SN ejecta form, suggesting a reduction in CSM density at  $r \gtrsim 10^{15}$  cm. The early time light curve of SN 2023ixf shows peak absolute magnitudes (e.g.,  $M_u = -18.6$  mag,  $M_g = -18.4$  mag) that are  $\gtrsim$ 2 mag brighter than typical type II SNe, this photometric boost also being consistent with the shock power supplied from CSM interaction. Comparison of SN 2023ixf to a grid of light-curve and multiepoch spectral models from the non-LTE radiative transfer code CMFGEN and the radiation-hydrodynamics code HERACLES suggests dense, solar-metallicity CSM confined to  $r = (0.5-1) \times 10^{15}$  cm, and a progenitor mass-

<sup>&</sup>lt;sup>31</sup> ISEF International Fellowship.



NSF Graduate Research Fellow.

loss rate of  $\dot{M} = 10^{-2} M_{\odot} \, \mathrm{yr}^{-1}$ . For the assumed progenitor wind velocity of  $v_w = 50 \, \mathrm{km \, s}^{-1}$ , this corresponds to enhanced mass loss (i.e., *superwind* phase) during the last  $\sim 3-6$  yr before explosion.

*Unified Astronomy Thesaurus concepts*: Core-collapse supernovae (304); Circumstellar matter (241); Red supergiant stars (1375); Sky surveys (1464)

Supporting material: data behind figures

#### 1. Introduction

A paramount issue in astrophysics is constraining how the lives of red supergiant (RSG) stars end. This avenue of study has a direct impact on the observed diversity of core-collapse supernovae (SNe), compact object formation, and element creation in the Universe. Advancing our understanding of latestage RSG evolution can be accomplished by probing the composition and structure of the circumstellar medium (CSM) surrounding these stars in the final years before explosion. This CSM is composed of material once located on the RSG surface and is enriched as the progenitor star loses mass via winds and/ or violent outbursts (Smith 2014). Understanding the structure of this CSM provides needed constraints on the final stages of stellar evolution before core collapse and the proposed mechanisms for both dynamic (e.g., gravity waves, super-Eddington winds; Owocki et al. 2004; Quataert & Shiode 2012; Quataert et al. 2016; Fuller 2017; Owocki et al. 2017; Wu & Fuller 2021) as well as secular (i.e., steady-state wind; Beasor et al. 2020) mass loss.

Early time, multiwavelength observations of young type II SNe (SNe II) are an essential probe of the final stages of stellar evolution; these last months to centuries are almost completely unconstrained in stellar evolutionary models. In the era of allsky transient surveys, "flash" or rapid spectroscopic observations have become a powerful tool in understanding the direct circumstellar environment of SN progenitors in the final months before explosion (e.g., Gal-Yam et al. 2014; Groh 2014; Smith et al. 2015; Khazov et al. 2016; Yaron et al. 2017; Jacobson-Galán et al. 2020; Bruch et al. 2021, 2023; Jacobson-Galán et al. 2022; Terreran et al. 2022; Tinyanont et al. 2022; Davis et al. 2023; Wang et al. 2023). Very early time spectra  $(t \le 7 \text{ days})$  can be used to identify prominent emission lines from the recombination of CSM photoionized by the incoming SN radiation at, and following, shock breakout. However, these spectral features are transient, leaving behind broad lines from the fastest ( $v_{ej} \approx 10^4 \text{ km s}^{-1}$ ) SN ejecta layers (Chugai 2001; Dessart et al. 2017). The strength of the narrow emission features depends on the CSM density and its chemical abundance. This is a robust tracer of the progenitor's chemical composition, identity, and recent mass loss at small distances  $(r < 10^{15})$  cm from the explosion; Gal-Yam et al. 2014; Dessart et al. 2017; Yaron et al. 2017; Boian & Groh 2020).

Spectroscopic modeling of CSM-interacting SNe II with non-LTE radiative transfer codes (e.g., CMFGEN; Hillier & Dessart 2012; Dessart et al. 2015) has been used to extract quantitative information on the progenitor's radius, chemical composition, wind velocity, and mass-loss rate. CMFGEN in particular allows for self-consistent post-processing of radiation hydrodynamics simulations, allowing for physically robust constraints on both the SN ejecta and CSM properties (shocked and unshocked) and the creation of accurate synthetic spectra that contain critical information absent from light curves. For example, CMFGEN spectral modeling of the prototypical "flash" spectroscopy type II SN 1998S indicated

an enhanced RSG mass-loss rate of  $\dot{M} \approx (0.6-1) \times 10^{-2} M_{\odot}$  $yr^{-1}$  ( $v_w \approx 50 \text{ km s}^{-1}$ ) in the final 15 yr before core collapse (Shivvers et al. 2015; Dessart et al. 2016). This mass-loss rate is significantly larger than that observed in galactic RSGs, e.g.,  $\dot{M} \approx 10^{-6} M_{\odot} \text{ yr}^{-1}$  (Beasor et al. 2020). Similarly, the modeling of the emission line spectrum in the first days of SNe 2017ahn and 2020pni (Tartaglia et al. 2021; Terreran et al. 2022) suggested N-rich CSM derived from mass-loss rates of  $\dot{M} \approx (3-6) \times 10^{-3} M_{\odot} \text{ yr}^{-1}$ . Further diversity was revealed from CMFGEN modeling of SN 2013fs (Yaron et al. 2017), observed within hours of explosion, which suggested a compact CSM ( $r < 3 \times 10^{14}$  cm) with a lower mass-loss rate of  $\dot{M} \approx (3-5) \times 10^{-3} M_{\odot} \text{ yr}^{-1}$  (Dessart et al. 2017). Additionally, both UV and/or optical photometry and the spectral series of SN 2020tlf were accurately modeled by CMFGEN simulations involving an inflated RSG progenitor  $(R_{\star} \approx 10^3 R_{\odot})$ , which exploded into a dense  $(\dot{M} = (1-3) \times 10^{-2} M_{\odot} \text{ yr}^{-1}, v_w = 50 \text{ km s}^{-1})$ , extended  $(r \approx 10^{15} \text{ m})$ cm) CSM; this scenario is also consistent with the detection of luminous precursor emission before explosion (Jacobson-Galán et al. 2022).

In this paper, we present, analyze, and model photometric and spectroscopic observations of SN 2023ixf, first reported to the Transient Name Server by Koichi Itagaki (Itagaki 2023) on 2023 May 19 (MJD 60083.90). SN 2023ixf was classified as a Type II SN (Perley et al. 2023) and is located at  $\alpha = 14^{\rm h}03^{\rm m}38.56, \delta = +54^{\circ}18.41.96$  in host galaxy Messier 101 (NGC 5457). Based on reported pre-discovery images from numerous observations of SN 2023ixf, we adopt a time of first light to be MJD  $60082.833 \pm 0.020$  (Mao et al. 2023) that is based on the average between last nondetection and first detection, but could be earlier given the shallow depth of the last nondetection limit. All phases reported in this paper are with respect to this adopted time of first light. In this paper, we use a redshift-independent host-galaxy distance  $6.85 \pm 0.15$  Mpc reported by Riess et al. (2022), which is the updated value beyond what is presented in Riess et al. (2016). We adopt a redshift of z = 0.000804 (Perley et al. 2023).

Given its close proximity and current relative brightness, SN 2023ixf represents an unparalleled opportunity to study both the very early time and the long-term evolution of a CSM-interacting SN II in unprecedented detail. In Section 2, we describe UV, optical, and NIR observations of SN 2023ixf. In Section 3, we present analysis, comparisons and modeling of SN 2023ixf's optical photometric and spectroscopic properties. Finally, in Section 4, we discuss the progenitor environment and mass-loss history prior to SN 2023ixf. Conclusions are drawn in Section 5. All uncertainties are quoted at the 68% confidence level unless otherwise stated.

## 2. Observations

## 2.1. Photometric Observations

SN 2023ixf was observed with the Pan-STARRS telescope (PS1/2; Kaiser et al. 2002; Chambers et al. 2017) between

2023 May 21 and June 2 in grizy bands through the Young Supernova Experiment (YSE; Jones et al. 2021). Data storage and/or visualization and follow-up coordination was done through the YSE-PZ web broker (Coulter et al. 2022, 2023). The YSE photometric pipeline is based on photpipe (Rest et al. 2005), which relies on calibrations from Magnier et al. (2020), Waters et al. (2020). Each image template was taken from stacked PS1 exposures, with most of the input data from the PS1  $3\pi$  survey. All images and templates were resampled and astrometrically aligned to match a skycell in the PS1 sky tessellation. An image zero-point is determined by comparing point-spread function (PSF) photometry of the stars to updated stellar catalogs of PS1 observations (Flewelling et al. 2020). The PS1 templates are convolved with a three-Gaussian kernel to match the PSF of the nightly images, and the convolved templates are subtracted from the nightly images with HOTPANTS (Becker 2015). Finally, a flux-weighted centroid is found for the position of the SN in each image, and PSF photometry is performed using forced photometry: the centroid of the PSF is forced to be at the SN position. The nightly zeropoint is applied to the photometry to determine the brightness of the SN for that epoch.

We obtained *ugri* imaging of SN 2023ixf with the Las Cumbres Observatory (LCO) 1 m telescopes from 2023 May 20 to June 1 (programs NSF2023A-011 and NSF2023A-015; PIs Foley and Kilpatrick, respectively). After downloading the BANZAI-reduced images from the LCO data archive (McCully et al. 2018), we used photpipe (Rest et al. 2005) to perform DoPhot PSF photometry (Schechter et al. 1993). All photometry was calibrated using PS1 stellar catalogs described above with additional transformations to SDSS u band derived from Finkbeiner et al. (2016). For additional details on our reductions, see Kilpatrick et al. (2018). We also obtained photometry using a 0.7 m Thai Robotic Telescope at Sierra Remote Observatories and the Nickel Telescope at Lick Observatory in the BVRI bands. Images are bias subtracted and field flattened. Absolute photometry is obtained using stars in the  $10' \times 10'$  field of view.

We also observed SN 2023ixf with the Lulin 1 m telescope in *griz* bands from 2023 May 21 to June 1. Standard calibrations for bias and flat-fielding were performed on the images using IRAF, and we reduced the calibrated frames in photpipe using the same methods described above for the LCO images.

We also observed SN 2023ixf with the Auburn 10" telescope located in Auburn, AL from 2023 May 27 to June 3 in *BGR* bands. Following standard procedures in python, we corrected each frame for bias, dark current, and flat-fielding using image frames obtained in the same instrumental setup. We then registered each frame using Gaia Data Release 3 astrometric standard stars (Gaia Collaboration 2022) observed in the same field as each image. Finally, we stacked images in each filter for each night with swarp and performed final photometry using DoPhot with calibration using Pan-STARRS *gri* standard stars transformed to *BVR* bands.<sup>32</sup> The complete multicolor light curve of SN 2023ixf is presented in Figure 1(a).

The Milky Way (MW) *V*-band extinction and color excess along the SN line of site is  $A_V = 0.025$  mag, and E(B-V) = 0.008 mag (Schlegel et al. 1998; Schlafly & Finkbeiner 2011), respectively, which we correct for using a standard Fitzpatrick (1999) reddening law ( $R_V = 3.1$ ). In addition to the MW color excess, we estimate the contribution of galaxy extinction in the local SN environment. Using a high resolution Kast spectrum of SN 2023ixf at  $\delta t = 2.4$  days, we calculate Na I D2 and D1 equivalent widths (EWs) of 0.16 and 0.12 Å, respectively; these values are consistent with those derived from a Keck Planet Finder spectrum (Lundquist et al. 2023). We use Equations (7) and (8) in Poznanski et al. (2012) to convert these EWs to an intrinsic E(B-V) and find a host galaxy extinction of  $E(B-V)_{host} = 0.033 \pm 0.010$  mag, also corrected for using the Fitzpatrick (1999) reddening law.

#### 2.2. Spectroscopic Observations

SN 2023ixf was observed with Shane/Kast (Miller & Stone 1993) between  $\delta t = 2.4$  and 14.4 days. For all these spectroscopic observations, standard CCD processing and spectrum extraction were accomplished with IRAF.<sup>33</sup> The data were extracted using the optimal algorithm of Horne (1986). Low-order polynomial fits to calibration-lamp spectra were used to establish the wavelength scale, and small adjustments derived from night-sky lines in the object frames were applied. SN 2023ixf spectra were also obtained with the Kitt Peak Ohio State Multi-Object Spectrograph (KOSMOS; Martini et al. 2014) on the Astrophysical Research Consortium 3.5 m Telescope at Apache Point Observatory (APO). The KOSMOS spectra were reduced through the KOSMOS<sup>34</sup> pipeline. One optical spectrum (in a red and blue arm) was taken through the Low-Resolution Spectrograph 2 (LRS2) instrument on the Hobby Eberly Telescope (HET) on 2023 May 21 (blue arm) and 2023 May 22 (red arm). The LRS2 data were processed with Panacea, 35 the HET automated reduction pipeline for LRS2. The initial processing includes bias correction, wavelength calibration, fiber-trace evaluation, fiber normalization, and fiber extraction; moreover, there is an initial flux calibration from default response curves, an estimation of the mirror illumination, as well as the exposure throughput from guider images. After the initial reduction, we use LRS2Multi<sup>36</sup> in order to perform sky subtraction.

In Figure 2, we present the complete series of optical spectroscopic observations of SN 2023ixf from  $\delta t = 2.4$  to 14.4 days. In this plot, we also show the classification spectrum of SN 2023ixf at +1.1 days from the Liverpool telescope (Perley et al. 2023). However, because we cannot verify the quality of this spectral reduction, we only use these data for narrow line identification. Additionally, we include Swift UV grism spectra of SN 2023ixf from  $\delta t = +1.8$  to 2.8 days in Appendix Figure 7; the data were reduced using the techniques outlined in Pan et al. (2020). The complete spectral sequence is shown in Figure 2, and the log of spectroscopic observations is presented in Appendix Table A1.

 $<sup>\</sup>overline{^{32}}$  Note that our *G*-band filter is close to Johnson *V* band, and so we calibrate against Pan-STARRS standard stars transformed into this band. For filter functions, see <a href="https://astronomy-imaging-camera.com/product/zwo-lrgb-31mm-filters-2">https://astronomy-imaging-camera.com/product/zwo-lrgb-31mm-filters-2</a>.

https://github.com/msiebert1/UCSC\_spectral\_pipeline

https://github.com/jradavenport/pykosmos

https://github.com/grzeimann/Panacea

<sup>36</sup> https://github.com/grzeimann/LRS2Multi

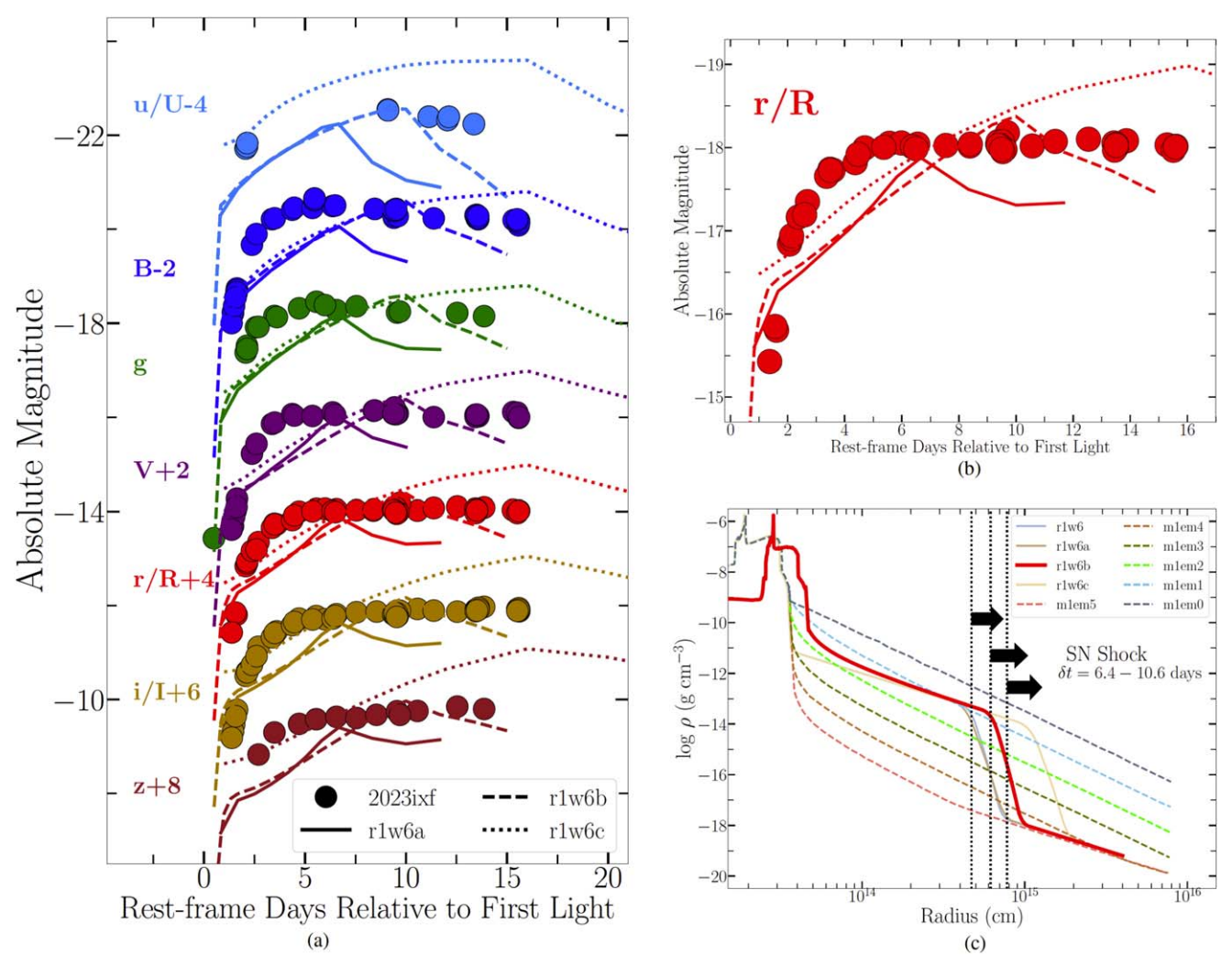


Figure 1. (a) Multicolor light curve of SN 2023ixf (circles) with respect to time since first light (MJD 60082.833  $\pm$  0.020) from PS1, LCO, Auburn, Thai Robotic Telescope, Nickel, and Lulin telescopes. Observed photometry is presented in the AB magnitude system and has been corrected for host galaxy and MW extinction. Light curves of CMFGEN models r1w6a ( $R_{\text{CSM}} = 6 \times 10^{14}$  cm,  $\dot{M} = 10^{-2} M_{\odot} \text{ yr}^{-1}$ ), r1w6b ( $R_{\text{CSM}} = 8 \times 10^{14}$  cm,  $\dot{M} = 10^{-2} M_{\odot} \text{ yr}^{-1}$ ), and r1w6c ( $R_{\text{CSM}} = 1 \times 10^{15}$  cm,  $\dot{M} = 10^{-2} M_{\odot} \text{ yr}^{-1}$ ) are plotted as solid, dashed, and dotted lines, respectively. (b) Zoom-in of the SN 2023ixf r- and/or R-band light curve and CMFGEN models, which can reproduce the peak magnitude but are inconsistent with the early time slope. (c) CSM densities and radii for a subset of the CMFGEN model grid (e.g., Table (A2)) used to find the best fitting model for SN 2023ixf, which is plotted as a solid red line (r1w6b). Dotted black lines represent lower limits on the location of the SN shock at  $\delta t = 6.4$ , 8.4, 10.6 days, for a lower limit on the SN shock velocity of  $\gtrsim$ 8500 km s<sup>-1</sup> (Section 3.2). We expect a decrease of the optical depth to electron-scattering (i.e.,  $\tau_{\text{ES}}$ ) based on the plotted density profile at around  $\sim$ 8 days, which is consistent with the fading of the IIn-like line profiles observed in SN 2023ixf at these phases.

(The data used to create this figure are available.)

## 3. Analysis

#### 3.1. Photometric Properties

The complete early time, multiband light curve of SN 2023ixf is presented in Figure 1(a). We fit a fifth-order polynomial to the g-band light curve to derive a peak absolute g-band magnitude of  $M_g = -18.4 \pm 0.10$  mag at MJD 60088.61  $\pm$  0.10, where the uncertainty on peak magnitude is the  $1\sigma$  error from the fit, and the uncertainty on the peak phase is found from adding the uncertainties on both the time of peak magnitude and the time of first light in quadrature. Using the adopted time of first light, this indicates a rise time of  $t_r = 5.8 \pm 0.10$  days with respect to g-band maximum. Other filters display similarly bright peak absolute magnitudes, e.g.,  $M_u = -18.6 \pm 0.11$  mag, and  $M_r = -18.0 \pm 0.09$  mag—this indicates a bolometric boost to the SN brightness rather than a

color effect. Following its rise to peak, the multicolor light curve of SN 2023ixf has remained at an approximately constant brightness, indicating that it could be entering a plateau phase (i.e., SN II-P classification). However, at this time, the SN is still very blue, therefore indicating that the recombination phase has yet to be reached. All peak magnitudes and rise-times are presented in Table 1.

In Figure 3, we compare the observed peak absolute magnitudes of SN 2023ixf to a sample of SNe II with spectroscopic signatures of CSM interaction (i.e., IIn-like profiles; W. V. Jacobson-Galán et al. 2023, in preparation). This gold sample includes most of the known CSM-interacting SNe II that show detectable IIn-like profiles in their early time spectra and have early time UV observations with Swift UVOT. The color delineation of all presented sample objects is as follows: at phases of  $t \sim 2$  days post-explosion, the blue

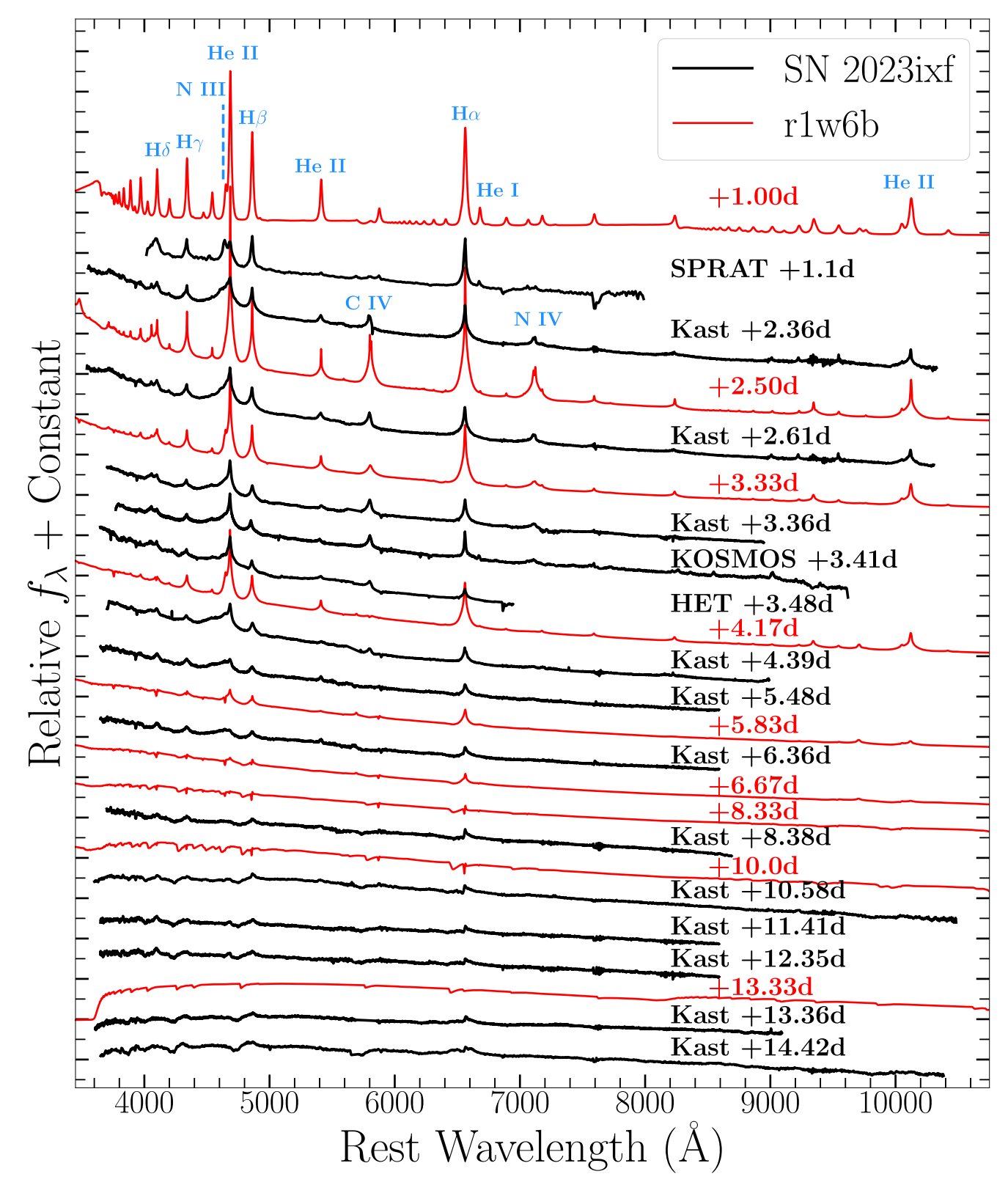
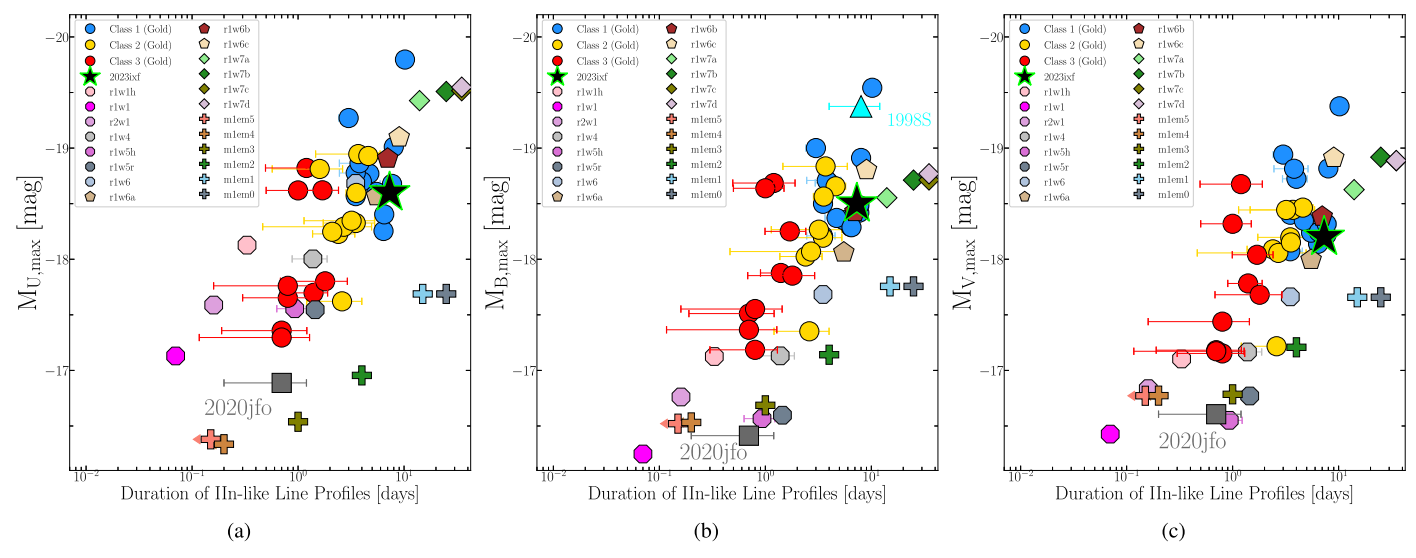


Figure 2. Early time spectral series of SN 2023ixf (black) with respect to CMFGEN model r1w6b (red), which is characterized by a wind mass-loss rate of  $\dot{M}=10^{-2}\,M_\odot$  yr $^{-1}$ , and that extends to a CSM radius of  $R_{\rm CSM}=8\times10^{14}$  cm. Model spectra have been smoothed with a Gaussian kernel to match the spectral resolution of the data. Line identifications shown in blue. The disappearance of He I and N III after the  $\delta t=+1.1$  day spectrum indicates a rise in ionization and temperature in SN 2023ixf following the propagation of the shock breakout radiation.

(The data used to create this figure are available.)



**Figure 3.** Peak (a) *U*-band, (b) *B*-band, and (c) *V*-band absolute magnitudes vs. duration of IIn-like line profiles ( $t_{\text{IIn}}$ ) for SN 2023ixf (black star) with respect to CSM-interacting SNe II presented in W. V. Jacobson-Galán et al. (2023, in preparation) shown as circles (color delineation discussed in Section 3.2). SN 2020jfo (Teja et al. 2022) shown as reference canonical SN II without significant CSM interaction (gray square). CMFGEN models plotted as colored octagons, polygons, diamonds, and plus signs. SN 2023ixf has an observed  $t_{\text{IIn}}$  and peak absolute magnitude that is consistent with the other gold sample SNe II displaying the strongest signs of CSM interaction, e.g., SNe 1998S, 2017ahn, 2020pni, 2020tlf (Leonard et al. 2000; Fassia et al. 2001; Shivvers et al. 2015; Tartaglia et al. 2021; Terreran et al. 2022; W. V. Jacobson-Galán et al. 2023, in preparation).

colored objects show high-ionization emission lines of NIII, He II, and C IV (e.g., SNe 1998S, 2017ahn, 2018zd, 2020pni, 2020tlf, etc.), the yellow colored objects have no N III emission but do show He II, and C IV (e.g., SNe 2014G, 2022jox), and the red colored objects only show weaker He II emission (e.g., SNe 2013fs). However, it should be noted that high-ionization lines of O V/VI, C V, and N IV are also present in SN 2013fs at t < 1 day due to a more compact CSM than other CSMinteracting SNe II (Dessart et al. 2017; Yaron et al. 2017). With respect to other SNe II with evidence for interaction with CSM, SN 2023ixf is  $\sim$ 0.5 mag brighter in all observed filters than the median peak absolute magnitude observed in the sample. SN 2023ixf has a comparable peak brightness and rise-times to those from SNe 2017ahn, 2018zd, 2020pni, 2020abjq, and 2022ffg (Zhang et al. 2020; Hiramatsu et al. 2021; Tartaglia et al. 2021; Terreran et al. 2022; W. V. Jacobson-Galán et al. 2023, in preparation), all of which have similar early time spectral morphology and duration of the IIn-like line profiles (Section 3.2). However, the rise-time of SN 2023ixf is significantly shorter than those from more extreme events such as SNe 1998S, 2019qch, 2020tlf, 2021tyw, and 2022pgf, whose rise-times are >12 days. This difference reflects a shorter interaction timescale in a less extended, high-density CSM in SN 2023ixf. Furthermore, SN 2023ixf is distinct from other prototypical SNe II with IIn-like profiles such as SN 2013fs and 2014G (Terreran et al. 2016; Yaron et al. 2017), which have shorter rise-times and lower peak absolute magnitudes. Finally, SN 2023ixf is  $\sim$ 2 mags brighter in multiband (i.e., uBVgriz) filters than SNe II without IIn-like profiles in their early time spectra e.g., SN 2020jfo (Teja et al. 2022; Figure 3) or average values derived from samples of SNe II (Anderson et al. 2014).

# 3.2. Spectroscopic Properties

The complete early time spectroscopic sequence of SN 2023ixf from  $\delta t = +1.1$  to +14.4 days is presented in Figure 2, consistent with other spectral sequences released on

Table 1
Main Parameters of SN 2023ixf

M101
0.000804
6.9 Mpc <sup>a</sup>
60082.83
0.008 mag <sup>b</sup>
0.033 mag <sup>c</sup>
-18.6  mag  [4.9  days]
-18.5  mag  [5.7  days]
-18.4  mag  [5.8  days]
-18.1  mag  [6.0  days]
-18.0  mag  [6.1  days]
-17.9  mag  [7.8  days]
-17.8  mag  [8.2  days]
$(0.5-1) \times 10^{15} \text{ cm}$
$(0.04-0.07)M_{\odot}$
$10^{-2} M_{\odot} \text{ yr}^{-1} [50 \text{ km s}^{-1}]$
Solar Metallicity <sup>e</sup>
$\sim$ 3–6 yr Pre-SN

#### Notes.

- <sup>a</sup> Riess et al. (2022).
- <sup>b</sup> Schlegel et al. (1998), Schlafly & Finkbeiner (2011).
- <sup>c</sup> Poznanski et al. (2012).
- <sup>d</sup> Mass loss within  $r < 10^{15}$  cm.
- <sup>e</sup> Not varied in model grid.

this object (Stritzinger et al. 2023; Yamanaka et al. 2023). In the earliest spectrum, SN 2023ixf shows narrow, symmetric emission features of H I, He I/II, N III/IV, and C IV. A two-component Lorentzian model fit to the H $\alpha$  profile in the high resolution ( $R \approx 3000$ ) +2.4 days Kast spectrum shows a narrow component full width at half maximum velocity of <150 km s<sup>-1</sup> and broad symmetric component velocity of  $\sim 1400$  km s<sup>-1</sup>; the former is ascribed to the progenitor wind while the latter is caused by scattering of recombination line photons by free, thermal electrons in the ionized CSM

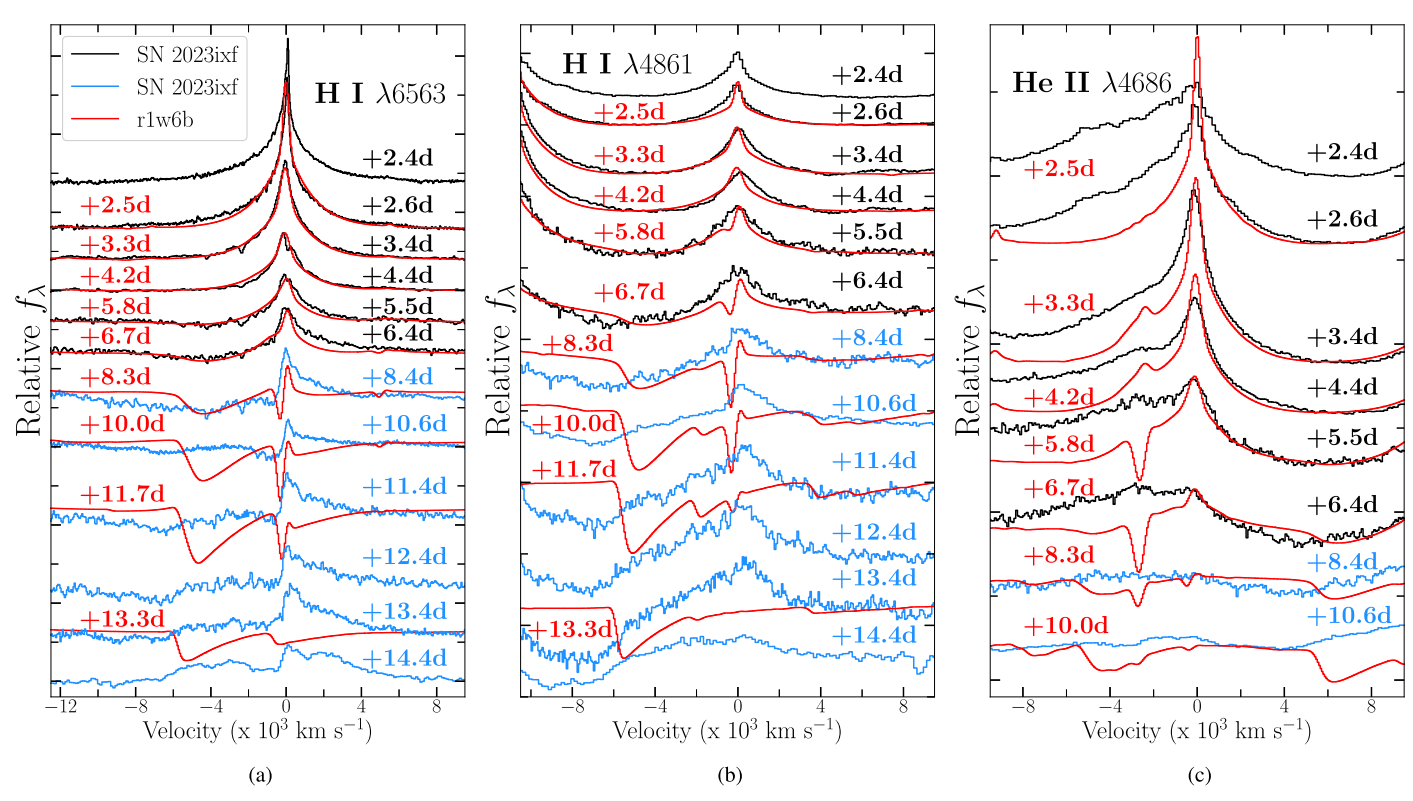


Figure 4. (a) H $\alpha$  velocity evolution in SN 2023ixf from  $\delta t = 2.4$  to 14.4 days with respect to r1w6b model spectra (red), which has been scaled to the emission line peaks of SN 2023ixf and smoothed with a Gaussian filter to better compare with the data. Early time spectral profiles are shaped by electron-scattering in the dense CSM. The transition shown from black to blue lines ( $t_{\text{IIn}} \approx 8$  days) marks the emergence of broad absorption features derived from the fastest moving SN ejecta. (b) H $\beta$  velocity evolution, also showing that the electron-scattering line profiles subside after  $\sim 8$  days. (c) He II  $\lambda 4686$  velocity evolution reveals that the electron-scattering profile fades by  $\sim 8$  days, suggesting a significant decrease in CSM density.

(Chugai 2001; Dessart et al. 2009; Huang & Chevalier 2018). However, it should be noted that, at these phases, there could be radiative acceleration of the CSM that causes the width of the narrow component to be larger than the true velocity of the progenitor wind (Dessart et al. 2015; Tsuna et al. 2023).

SN 2023ixf may be the first SN to exhibit a rapid rise in ionization between the first and second spectrum as shown in Figure 2. This is caused initially by the shock breakout pulse and later on by the incoming radiation from the embedded shock. This is witnessed here with the presence of lines of moderately ionized species (i.e., lines of He I or N III) and a moderately blue color at  $\delta t=1.1$  days. At  $\delta t=2.4$  days, the SN 2023ixf spectrum is much bluer, the lines of He I  $\lambda\lambda\lambda$  5875, 6678, and 7065 have weakened or disappeared, and the spectrum exhibits instead lines of C IV ( $\lambda5808$ ) and He II ( $\lambda4686$ ). Furthermore, there is emission from N V  $\lambda4604$  to 4620 contributing at the wavelengths bluewards of the He II  $\lambda4686$  line, consistent with heightened ionization at these phases.

The narrow, symmetric line profiles with Lorentzian wings caused by electron-scattering (i.e., IIn-like) continue to persist in SN 2023ixf for the first week of the SN evolution. Then, in the +5.48 and +6.36 days spectra, the He II emission begins to fade (Figure 4), and the SN develops a broad absorption profile in all Balmer transitions, indicating the escape of photons from the fast-moving ejecta and a decrease in CSM density. We therefore define the duration of the IIn-like line profiles as the transition point at which the optical depth to electron-scattering has dropped enough to see the emerging fast-moving SN ejecta. For SN 2023ixf, we estimate that this change occurs at  $t_{\rm IIn}\approx 8$  days, which is reflective of the disappearance of the electron-scattering wings in the He II emission line and the development

of broad absorption profiles at Balmer series wavelengths. This indicates that the photosphere is first located in the unshocked CSM (far above the shock), then in the swept up material present in the fast-moving dense shell (i.e., shocked CSM), and then in the fastest moving SN ejecta below the dense shell. Based on the  $T > 10 \, \mathrm{keV}$  X-ray spectrum of SN 2023ixf (Grefenstette et al. 2023), there is sufficiently high temperatures for He II to exist, so the decrease in line strength can be attributed to a reduction in particle density as the shock samples CSM at  $r > 10^{15} \, \mathrm{cm}$ . As shown in Figure 4, the bluest edge of the H $\alpha$  and H $\beta$  line profiles corresponds to velocities of  $\sim 8500 \, \mathrm{km \, s^{-1}}$ , which provides a lower limit on the velocities of the fastest moving H-rich material at the shock front. By two weeks post-explosion, the SN spectra is composed of broad H I absorption profiles, similar to other young SNe II.

The duration of the IIn-like signatures in SN 2023ixf is consistent with other CSM-interacting SNe II with enhanced progenitor mass-loss rates of  $\dot{M} > 10^{-2} M_{\odot} \text{ yr}^{-1}$  (Figure 3). In Figure 3, we present peak absolute magnitudes with respect to IIn profile duration for all gold sample CSM-interacting SNe II analyzed in W. V. Jacobson-Galán et al. (2023, in preparation). Intriguingly, there exists a natural trend between peak brightness and IIn-like profile duration among these events, which is reflective of a continuum of progenitor mass-loss rate and CSM extent. The observed  $t_{\text{IIn}}$  in SN 2023ixf is most similar to SNe 2017ahn, 2018zd, 2020pni, 2020tlf, and 2022ffg, but is not as large as that observed in 2020tlf, 2021tyw, or 2022pgf, likely due to a more extended dense CSM in those objects. Furthermore, the evolution of SN 2023ixf is unlike other CSM-interacting SNe II with  $t_{\rm IIn}$  < 5 days post-explosion (e.g., SNe 2013fs or 2014G), which do not show N emission lines at

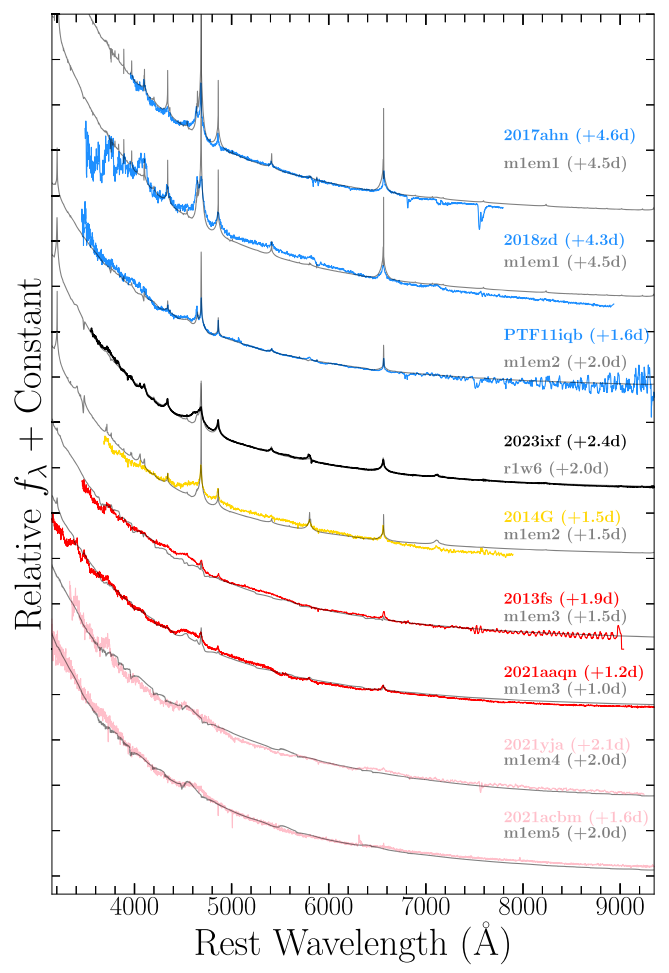


**Figure 5.** Early time spectra of SNe II with varying degrees of CSM interaction, selected from W. V. Jacobson-Galán et al. (2023, in preparation). Colors delineate differences between duration of IIn-like signatures as well as the presence of different high-ionization species at phases of  $t \approx 2$  days (e.g., spectra in blue show N III while others do not). Overplotted in gray are best fitting CMFGEN models for high  $(10^{-1}\,M_\odot\,\,\rm yr^{-1};$  top) to low  $(10^{-5}\,M_\odot\,\,\rm yr^{-1};$  bottom) mass-loss rates. SN 2023ixf lies within the continuum of CSM-interacting SNe II, and the evolution of its prominent spectral signatures of photoionized CSM is consistent with a progenitor mass-loss rate of  $\dot{M}=10^{-2}\,M_\odot\,\,\rm yr^{-1}$ .

phases >1 day post-explosion and are caused by a more compact and/or high-density CSM or extended and/or low-density CSM (Dessart et al. 2017). The observed early spectral differences between SN 2023ixf and other CSM-interacting SNe II are illustrated in Figure 5. Here, it is shown that the line profiles of SN 2023ixf at  $\sim$ 2 days post-explosion are most consistent with interaction between SN ejecta and CSM constructed from a high progenitor mass-loss rate  $(\dot{M}>10^{-2}\,M_{\odot}~{\rm yr}^{-1};$  also see Figure 6).

## 3.3. Modeling

In order to quantify the CSM properties of SN 2023ixf, we compared the spectral and photometric properties of SN 2023ixf to a model grid of non-LTE, radiative transfer simulations covering a wide range of progenitor mass-loss rates  $(\dot{M}=10^{-6}-10^0~M_{\odot}~{\rm yr}^{-1};~\nu_w=50~{\rm km~s}^{-1})$  and CSM radii  $(R=10^{14}-10^{16}~{\rm cm})$ , all in spherical symmetry. The simulations of the SN ejecta–SM interaction were performed with the multi-group radiation-hydrodynamics code HERACLES

(González et al. 2007; Vaytet et al. 2011; Dessart et al. 2015), which consistently computes the radiation field and hydrodynamics. Then, at selected snapshots in time postexplosion, the hydrodynamical variables are imported into the non-LTE radiative-transfer code CMFGEN (Hillier & Dessart 2012; Dessart et al. 2015) for an accurate calculation of the radiative transfer, which includes a complete model atom,  $\sim 10^6$  frequency points, and treatment of continuum and line processes as well as electron-scattering. For each model, we adopt an explosion energy of  $1.2 \times 10^{51}$  erg, a  $15M_{\odot}$  progenitor with a radius ranging from  $R_{\star} \approx 500$  to  $700 R_{\odot}$ , and a CSM composition set to the surface mixture of a RSG progenitor (Davies & Dessart 2019). For the simulations presented in this work, the CSM extent is much greater than  $R_{\star}$  $(\sim 500-1200 R_{\odot})$  for a RSG mass range of  $\sim 10-20 M_{\odot}$ , and therefore, the progenitor properties have no impact during phases of ejecta-CSM interaction. The progenitor radius plays a more significant role on the light-curve evolution during the plateau phase (e.g., see Dessart et al. 2013; Jacobson-Galán et al. 2022), i.e., once the interaction phase is over and the emission from from the deeper ejecta layers dominate the SN luminosity. Specific methods for each simulation can be found in Dessart et al. (2016), Dessart et al. (2017), Jacobson-Galán et al. (2022), and Dessart & Jacobson-Galán (2023), and all CSM properties of each model are presented in Table A2.

From the CMFGEN model grid, we identify four models (r1w6, r1w6a, b, c) with the smallest residuals between model predictions and both the observed multicolor peak magnitudes and rise-times (Section 3.1) as well as the duration of IIn profiles (Section 3.2). The best matched model peak magnitudes are within  $\sim$ 0.5 mag of SN 2023ixf in all filters and have a  $t_{\text{IIn}}$  that is within  $\pm 3$  days of that observed in SN 2023ixf. The features used for determination of the most consistent model are presented in Figure 3. We find that the best-fit models to SN 2023ixf have a mass-loss rate of  $\dot{M}=10^{-2}\,M_{\odot}~{\rm yr}^{-1}$ , confined to a radius of  $r=(0.5\text{--}1)\times10^{15}$ cm, and containing a total CSM mass of  $M_{\rm CSM} \approx 0.04 - 0.07 \, M_{\odot}$ . Based on model predictions, the mass loss then decreases to  $\dot{M} = 10^{-6} M_{\odot} \text{ yr}^{-1}$  (e.g., Figure 1(b)) at larger distances  $(r > 10^{15} \text{ cm})$ , with a constant wind velocity of  $v_w = 50 \,\mathrm{km \, s^{-1}}$ ; this geometry is consistent with the changing X-ray absorption observed in SN 2023ixf (Grefenstette et al. 2023). This wind velocity is not derived from spectroscopic observations, but the narrow line cores of the higher resolution Kast spectra indicate  $v_w \lesssim 150 \, \mathrm{km \, s^{-1}}$ . The spectral time series of the rlw6b model and multicolor light curve of the rlw6a, b, c models are presented in Figures 2 and 1(a). In Figure 6, we present SN 2023ixf spectra with respect to a range of early time CMFGEN models with varying mass-loss rates and CSM radii to further illustrate the consistencies and inconsistencies between models and observations. In Figure 7, we present the UV spectrum of the r1w6b at +2.5 days, which predicts a plethora of high-ionization features (e.g., O IV/VI) in the near-to-far-UV spectra of SN 2023ixf. Furthermore, the r1w6b model adequately reproduces the observed IIn-like emission line profiles in SN 2023ixf (e.g., Figures 5 and 6) using the  $15 M_{\odot}$ , solar metallicity, RSG progenitor model composition (Dessart et al. 2017; Davies & Dessart 2019).

Unlike the other CSM structures explored in the CMFGEN model grid, the r1w6b model best reproduces both the observed peak absolute magnitudes in *uBgVriz* filters as well as the duration of IIn-like line profiles observed in SN 2023ixf (Figure 3). However, this model cannot match the early light-

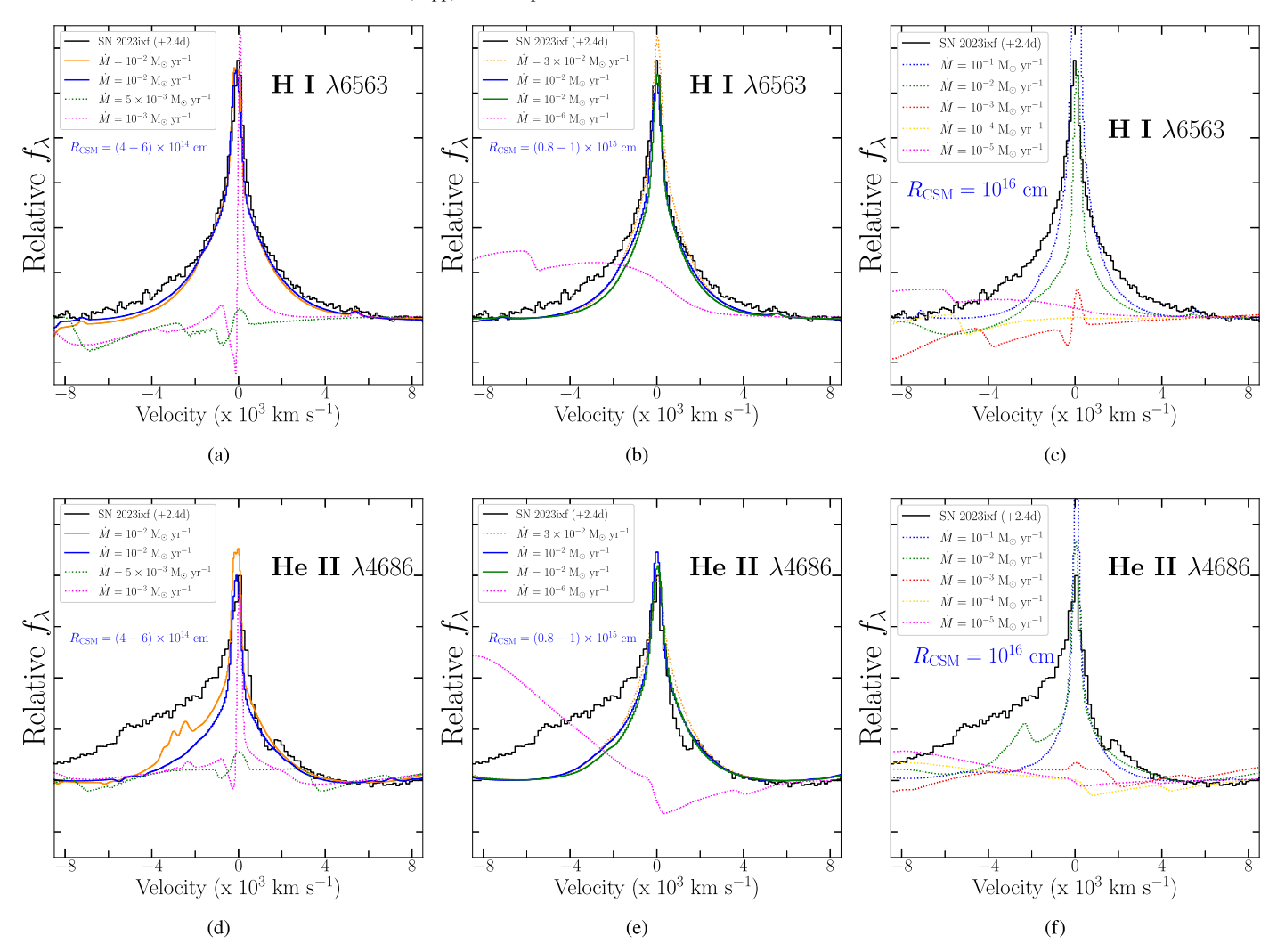


Figure 6. H $\alpha$  velocity of SN 2023ixf at  $\delta t = 2.4$  days (black) with respect to CMFGEN model spectra at +2 days post-explosion. Best-fit models (e.g., Section 3.3) shown as solid lines; additional, inconsistent models plotted as dotted lines. For proper comparison, models are scaled to the continuum of SN 2023ixf and the peak of the presented emission line profile. These models have varying mass-loss rates that are contained within CSM radii of (a)  $R_{\text{CSM}} = (4-6) \times 10^{14}$  cm, (b)  $R_{\text{CSM}} = (0.8-1) \times 10^{15}$  cm, and (c)  $R_{\text{CSM}} = 10^{16}$  cm. (d), (e), (f) Same as above, but for He II velocities.

curve slope observed in SN 2023ixf, which is likely a result of the density profile invoked. A better fit to the light curve would require a higher density immediately above  $R_{\star}$  (e.g., through a larger scale height) and a more gradual decline in density at the outer edge of the dense CSM, i.e., at  $\sim 8 \times 10^{15}$  cm. A more extended CSM, as in model r1w6c, increases the rise time to maximum and is thus not a suitable solution. Furthermore, a larger model kinetic energy will also increase the luminosity at early times, which would provide more consistency between the model light-curve rise and that from SN 2023ixf.

The evolution of the line profiles in the r1w6b model are consistent with the observed transition from electron-scattering broadened line profiles of Balmer series H I, He II, C IV, and N III/IV (t < 7 days) to Doppler broadened absorption profiles of the fastest moving H-rich SN ejecta (t > 7 days). Nevertheless, for a consistent continuum slope, the model spectra overpredict the narrow line emission observed in SN 2023ixf (e.g., Figure 2), which is likely caused by a smaller emitting volume of dense CSM in SN 2023ixf than the r1w6b model. The line strengths of SN 2023ixf are well-matched by the r1w6 model, which is characterized by the same  $\dot{M}$  but smaller CSM radius (e.g., Figure 5); this model, however, is unable to

reproduce the extended duration of the IIn-like features (e.g., see Figure 3). Furthermore, as shown in Figure 4(c), the He II  $\lambda$ 4686 line profile is not completely reproduced by the model spectrum, which could be due to the fact that these simulations are performed in 1D, assume spherical symmetry of the CSM, or require higher kinetic energies. Additionally, once the IIn-like profiles fade, the model H I ejecta velocities are lower than in SN 2023ixf (e.g., Figure 4). It should also be noted that the narrow H $\alpha$  P Cygni profile that develops in SN 2023ixf at t>8 days has higher velocities ( $\sim$ 100 km s<sup>-1</sup>) than those of the r1w6b model ( $\sim$ 50 km s<sup>-1</sup>), suggesting potential radiative acceleration of the unshocked CSM.

Using the lower limit on the SN shock velocity of  $\gtrsim 8500 \,\mathrm{km \, s^{-1}}$  as observed at the bluest edge of the H $\alpha$  absorption profile shown in Figure 4, we find that the location of the SN shock at t = 6.4 days is  $r \gtrsim 5 \times 10^{14}$  cm, which corresponds to an optical depth to electron-scattering of  $\tau \approx 10$  in the r1w6b model. Then, by t = 10.6 days, the shock is located at  $r \gtrsim 8 \times 10^{14}$  cm, which, in the r1w6b model, is in CSM with an electron-scattering optical depth of  $\tau \approx 0.2$ . This decrease in  $\tau_{\rm ES}$  in the r1w6b model is consistent with the observed fading of IIn-like profiles in

SN 2023ixf and reflects a reduction in CSM density at  $r > 10^{15}$  cm. However, it should be noted that the shock velocity decreases as the shock crosses the CSM, and therefore, the shock position is not as simplified as  $R_{\rm sh} = v_{\rm sh} \times t$ . We present the time-series evolution of the r1w6b model luminosity, density, temperature, and velocity as a function of radius in Figure 8. Furthermore, at +15 days, the r1w6b model has a maximum ejecta velocity of  $\sim$ 6500 km s<sup>-1</sup>, which is below the maximum velocities observed in the H $\alpha$  profile of SN 2023ixf. This may indicate some degree of CSM asymmetry that would cause a deceleration along certain lines of sight while also allowing for typical SN ejecta velocities of  $\sim 10^4 \,\mathrm{km \, s^{-1}}$  to be preserved. Also, the weaker Doppler broadened absorption observed in SN 2023ixf compared to the r1w6b model may be the result of persistent CSM interaction that will contribute weak, broad, and boxy H $\alpha$  emission capable of reducing the absorption profile strength (Dessart & Hillier 2022).

## 4. Discussion

The first 2 weeks of photometric and spectroscopic observations of SN 2023ixf have revealed essential characteristics of the SN progenitor system and the explosion itself. Based on the best fitting CMFGEN model, the progenitor of SN 2023ixf was likely a RSG with a mass-loss rate of  $\dot{M} \approx 10^{-2}\,M_\odot$  yr<sup>-1</sup>, which created dense CSM extending to  $r\approx (0.5-1)\times 10^{15}\,$  cm that contained a total mass of  $M_{\rm CSM}\approx 0.04-0.07\,M_\odot$ . Furthermore, we find that the observed light curve can be fit with standard explosion energy  $(1.2\times 10^{51}\,{\rm erg})$  and that the IIn-like signatures in SN 2023ixf can be modeled with a CSM composition that matches typical RSG surface abundances with no need for significant N or He enrichment.

For a wind velocity of  $\sim 50 \, \mathrm{km \, s^{-1}}$ , the proposed CSM extent translates to a period of enhanced mass loss (i.e., *superwind*) in the last  $\sim$ 3–6 yr prior to core collapse. This scenario comports with the observed duration of SN 2023ixf's IIn-like line profiles (~8 days), after which time the optical depth to electron-scattering in the CSM has decreased, and SN 2023ixf begins to show absorption profiles from the outer, H-rich ejecta and fast-moving dense shell. If the CSM detected in SN 2023ixf represents the only high-density shell of CSM (i.e., only one super wind phase), then the SN shock should continue to sample low-density material ( $\dot{M} \approx 10^{-6} M_{\odot} \text{ yr}^{-1}$ ,  $v_w = 50 \text{ km s}^{-1}$ ) at larger distances  $(r > 10^{15} \text{ cm})$ . Overall, both the confined high-density CSM shell and the extended lowdensity wind may have made the RSG progenitor star quite dust obscured prior to the explosion (Davies et al. 2022). This is consistent with the findings of Kilpatrick et al. (2023) who show that the pre-explosion Hubble and Spitzer imaging of SN 2023ixf indicates a moderately sized ( $\sim$ 11  $M_{\odot}$ ) RSG progenitor star enshrouded in a dust shell.

This physical progenitor picture is also consistent with the initial findings of multiwavelength observations of SN 2023ixf. X-ray observations revealed a 3–30 keV spectrum consistent with bremsstrahlung emission that initially showed significant absorption in the soft part of the spectrum (Grefenstette et al. 2023). These observations are indicative of shock interaction with dense CSM in a confined shell. Furthermore, radio observations have so far produced nondetections at  $\nu = 1$ –230 GHz with Submillimeter Array, GMRT, and Very

Large Array (Berger et al. 2023; Chandra et al. 2023; Matthews et al. 2023), likely caused by large free–free absorption in the optically thick CSM. However, as the SN shock now enters lower-density material at larger distances, it is probable that the radio emission in SN 2023ixf will become detectable.

## 5. Conclusions

In this paper, we have presented UV and/or optical observations and models of the nearby SN II, 2023ixf located in nearby spiral host galaxy M101 at d=6.9 Mpc. Below, we summarize the primary observational findings of SN 2023ixf:

- 1. The early time spectra of SN 2023ixf show prominent narrow emission lines of H I, He I/II, N III/IV/V, and C IV that result from the photoionization of dense, optically thick CSM. These electron-scattering broadened profiles (i.e., IIn-like) last for  $t_{\rm IIn} \approx 8$  days, after which time broad absorption profiles from the fastest H-rich SN ejecta begin to form.
- 2. CSM interaction in SN 2023ixf caused increased peak absolute magnitudes (e.g.,  $M_u = -18.6$  mag,  $M_g = -18.4$  mag) relative to SNe II that occur in a low-density circumstellar environment (e.g.,  $\rho < 10^{-16}$  g cm<sup>-3</sup>). The observed multicolor peak absolute magnitudes and duration of the IIn-like profiles (i.e.,  $t_{\rm IIn}$ ) place SN 2023ixf in the continuum of SNe II with varying degrees of RSG mass loss before explosion. Compared to the sample of CSM-interacting SNe II compiled in W. V. Jacobson-Galán et al. (2023, in preparation), SN 2023ixf is most similar to SNe 2017ahn, 2018zd, 2020pni, and 2022ffg.
- 3. Comparing SN 2023ixf's peak absolute magnitudes and duration of IIn-like profiles to a grid of CMFGEN simulations suggests a CSM that has a composition typical of a solar-metallicity RSG, is confined to  $r \approx (0.5-1) \times 10^{15}$  cm, and is formed from wind corresponding to a progenitor mass-loss rate of  $\dot{M} = 10^{-2}\,M_\odot$  yr<sup>-1</sup> (i.e.,  $\rho \approx 10^{-12}$  g cm<sup>-3</sup> at  $r = 10^{14}$  cm). Adopting a wind velocity of  $v_w = 50\,\mathrm{km\,s^{-1}}$ , this scenario corresponds to a period of enhanced mass loss (i.e., *superwind*) during the last  $\sim 3-6$  yr before core collapse.

Given its close proximity and present brightness, SN 2023ixf is poised to become the best studied CSM-interacting SN II to date. Future, multiwavelength observations will, among other things, uncover the density profile of the confined CSM as well as the mass-loss history of the RSG progenitor in its final decades to centuries.

# Acknowledgments

Research at UC Berkeley is conducted on the territory of Huichin, the ancestral and unceded land of the Chochenyo speaking Ohlone people, the successors of the sovereign Verona Band of Alameda County. PS1/2 observations were conducted on the stolen land of the kānaka 'õiwi people. We stand in solidarity with the Pu'uhonua o Pu'uhuluhulu Maunakea in their effort to preserve these sacred spaces for native Hawai'ians. Shane 3 m observations were conducted on the stolen land of the Ohlone (Costanoans), Tamyen, and Muwekma Ohlone tribes.

We thank Greg Zeimann for help with HET data reduction and Dan Weisz for Kast observations.

The Young Supernova Experiment and its research infrastructure are supported by the European Research Council under the European Union's Horizon 2020 research and innovation program (ERC Grant Agreement No. 101002652, PI K. Mandel), the Heising-Simons Foundation (2018-0913, PI R. Foley; 2018-0911, PI R. Margutti), NASA (NNG17PX03C, PI R. Foley), NSF (AST-1720756, AST-1815935, PI R. Foley; AST-1909796, AST-1944985, PI R. Margutti), the David & Lucille Packard Foundation (PI R. Foley), VILLUM FONDEN (project No. 16599, PI J. Hjorth), and the Center for AstroPhysical Surveys (CAPS) at the National Center for Supercomputing Applications (NCSA) and the University of Illinois Urbana-Champaign.

W.J.-G. is supported by the National Science Foundation Graduate Research Fellowship Program under grant No. DGE-1842165. W.J.-G. acknowledges support through NASA grants in support of Hubble Space Telescope (HST) program GO-16075 and 16500. This research was supported in part by the National Science Foundation under grant No. NSF PHY-1748958. R.M. acknowledges support by the National Science Foundation under award No. AST-2221789 and AST-2224255. The Margutti team at UC Berkeley is partially funded by the Heising-Simons Foundation under grant Nos. 2018-0911 and 2021-3248 (PI: Margutti).

C.D.K. is partly supported by a CIERA postdoctoral fellowship and a grant in support of NASA program HST-GO-16136. V.A.V. acknowledges support by the National Science Foundation under award No. AST-2108676. C.R.A. was supported by grants from VILLUM FONDEN (project No. 16599). Parts of this research were supported by the Australian Research Council Centre of Excellence for All Sky Astrophysics in 3D (ASTRO 3D), through project No. CE170100013. Y.-C.P. is supported by the National Science and Technology Council (NSTC) grant 109-2112-M-008-031-MY3. A.G. is supported by the National Science Foundation Graduate Research Fellowship Program under grant No. DGE-1746047. A.G. also acknowledges funding from the Center for Astrophysical Surveys Fellowship at UIUC/NCSA and the Illinois Distinguished Fellowship. C.G. is supported by a VILLUM FONDEN Young Investigator grant (project No. 25501). S.J.S. acknowledges funding from STFC grants ref: ST/T000198/1 and ST/S006109/1. J.H. was supported by a VILLUM FONDEN Investigator grant (project No. 16599). D. M. acknowledges NSF support from grants PHY-2209451 and AST-2206532.

The UCSC team is supported in part by NASA grants NNG17PX03C and 80NSSC22K1518, NSF grant AST-1815935, and a fellowship from the David and Lucile Packard Foundation to R.J.F.

YSE-PZ (Coulter et al. 2023) was developed by the UC Santa Cruz Transients Team with support from NASA grants NNG17PX03C, 80NSSC19K1386, and 80NSSC20K0953; NSF grants AST-1518052, AST-1815935, and AST-1911206; the Gordon & Betty Moore Foundation; the Heising-Simons Foundation; a fellowship from the David and Lucile Packard Foundation to R.J.F.; Gordon and Betty Moore

Foundation postdoctoral fellowships and a NASA Einstein fellowship, as administered through the NASA Hubble Fellowship program and grant HST-HF2-51462.001, to D.O.J.; and a National Science Foundation Graduate Research Fellowship, administered through grant No. DGE-1339067, to D.A.C.

A major upgrade of the Kast spectrograph on the Shane 3 m telescope at Lick Observatory, led by Brad Holden, was made possible through generous gifts from the Heising-Simons Foundation, William and Marina Kast, and the University of California Observatories. Research at Lick Observatory is partially supported by a generous gift from Google.

This research was supported by the Munich Institute for Astro-, Particle and BioPhysics (MIAPbP), which is funded by the Deutsche Forschungsgemeinschaft (DFG, German Research Foundation) under Germany's Excellence Strategy—EXC-2094—390783311.

This work was granted access to the HPC resources of TGCC under the allocation 2022–A0130410554 made by GENCI, France.

The Pan-STARRS1 Surveys (PS1) and the PS1 public science archive have been made possible through contributions by the Institute for Astronomy, the University of Hawaii, the Pan-STARRS Project Office, the Max-Planck Society and its participating institutes, the Max Planck Institute for Astronomy, Heidelberg and the Max Planck Institute for Extraterrestrial Physics, Garching, The Johns Hopkins University, Durham University, the University of Edinburgh, the Queen's University Belfast, the Harvard-Smithsonian Center for Astrophysics, the Las Cumbres Observatory Global Telescope Network Incorporated, the National Central University of Taiwan, STScI, NASA under grant NNX08AR22G issued through the Planetary Science Division of the NASA Science Mission Directorate, NSF grant AST-1238877, the University of Maryland, Eotvos Lorand University (ELTE), the Los Alamos National Laboratory, and the Gordon and Betty Moore Foundation.

IRAF is distributed by NOAO, which is operated by AURA, Inc., under cooperative agreement with the National Science Foundation (NSF).

Facilities: PS1, Shane (Kast Double spectrograph), Nickel Telescope, Las Cumbres Observatory, Lulin Telescope, HET (LRS), APO (KOSMOS).

Software: IRAF (Tody 1986; Tody 1993), photpipe (Rest et al. 2005), DoPhot (Schechter et al. 1993), HOTPANTS (Becker 2015), YSE-PZ (Coulter et al. 2022, 2023), CMFGEN (Hillier & Dessart 2012; Dessart et al. 2015), HERACLES (González et al. 2007; Vaytet et al. 2011; Dessart et al. 2015).

## **Appendix**

Here, we present a log of optical spectroscopic observations of SN 2023ixf in Table A1 and a list of model properties for all CMFGEN simulations in Table A2. Figure 7 presents Swift UVOT grism spectra of SN 2023ixf and model predictions for far-UV spectral features. Figure 8 shows the time-series evolution of luminosity, density, temperature, and velocity as a function of radius in the r1w6b model.

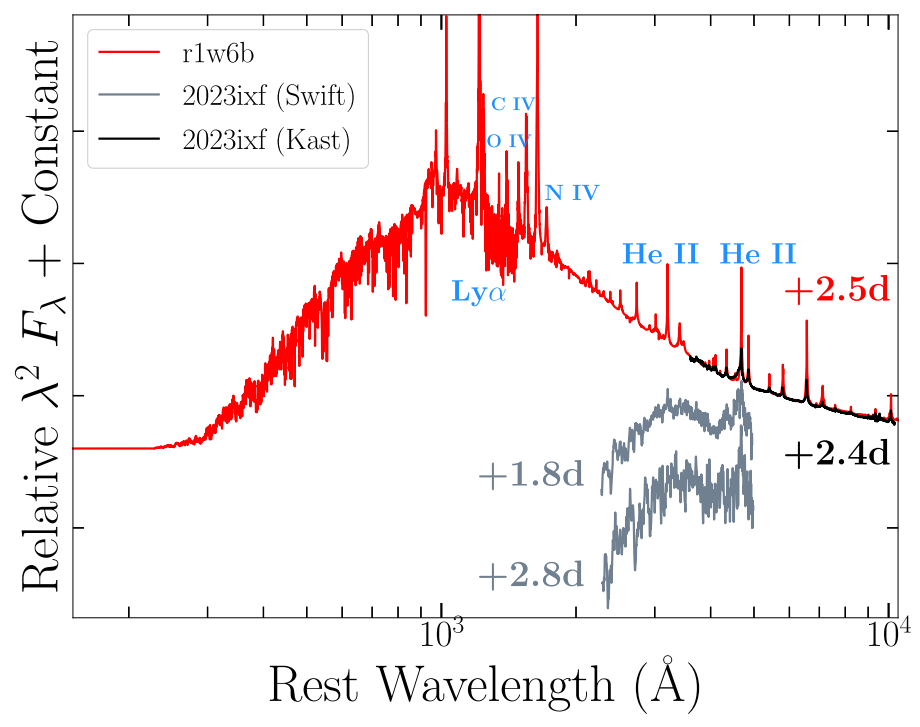


Figure 7. Swift UV grism spectra (gray) with respect to best fitting CMFGEN model (red); y-axis is in units of  $\lambda^2 F_{\lambda}$ . The Swift UV grism response function below  $\sim$ 3200 Å is not reflective of the true slope of the SN spectral energy distribution. The r1w6b model shows that the near-UV and far-UV spectra of SN 2023ixf likely contain a plethora of narrow, high-ionization emission lines (e.g., He II, C IV, N IV/V, and O IV) derived from CSM interaction.

**Table A1**Optical Spectroscopy of SN 2023ixf

UT Date	MJD	Phase <sup>a</sup> (days)	Telescope	Instrument	Wavelength Range (Å)
2023-05-21	60085.20	2.36	Shane	Kast	3600-10,800
2023-05-21	60085.21	2.37	Shane	Kast	5600-7254
2023-05-21	60085.44	2.61	Shane	Kast	3600-10,800
2023-05-21	60085.46	2.63	Shane	Kast	5600-7254
2023-05-22	60086.20	3.36	Shane	Kast	3600-9000
2023-05-22	60086.24	3.41	APO	KOSMOS	3600-10,800
2023-05-22	60086.31	3.48	HET	LRS	3600-7000
2023-05-23	60087.23	4.39	Shane	Kast	3600-9000
2023-05-24	60088.31	5.48	Shane	Kast	3600-9000
2023-05-25	60089.20	6.36	Shane	Kast	3600-9000
2023-05-27	60091.21	8.38	Shane	Kast	3600-9000
2023-05-29	60093.41	10.58	Shane	Kast	3600-10,800
2023-05-29	60093.42	10.59	Shane	Kast	5600-7254
2023-05-30	60094.25	11.41	Shane	Kast	3600-9000
2023-05-31	60095.19	12.35	Shane	Kast	3600-9000
2023-06-02	60097.26	14.43	Shane	Kast	3600-10,800

#### Note

<sup>&</sup>lt;sup>a</sup> Relative to first light (MJD 60082.83).

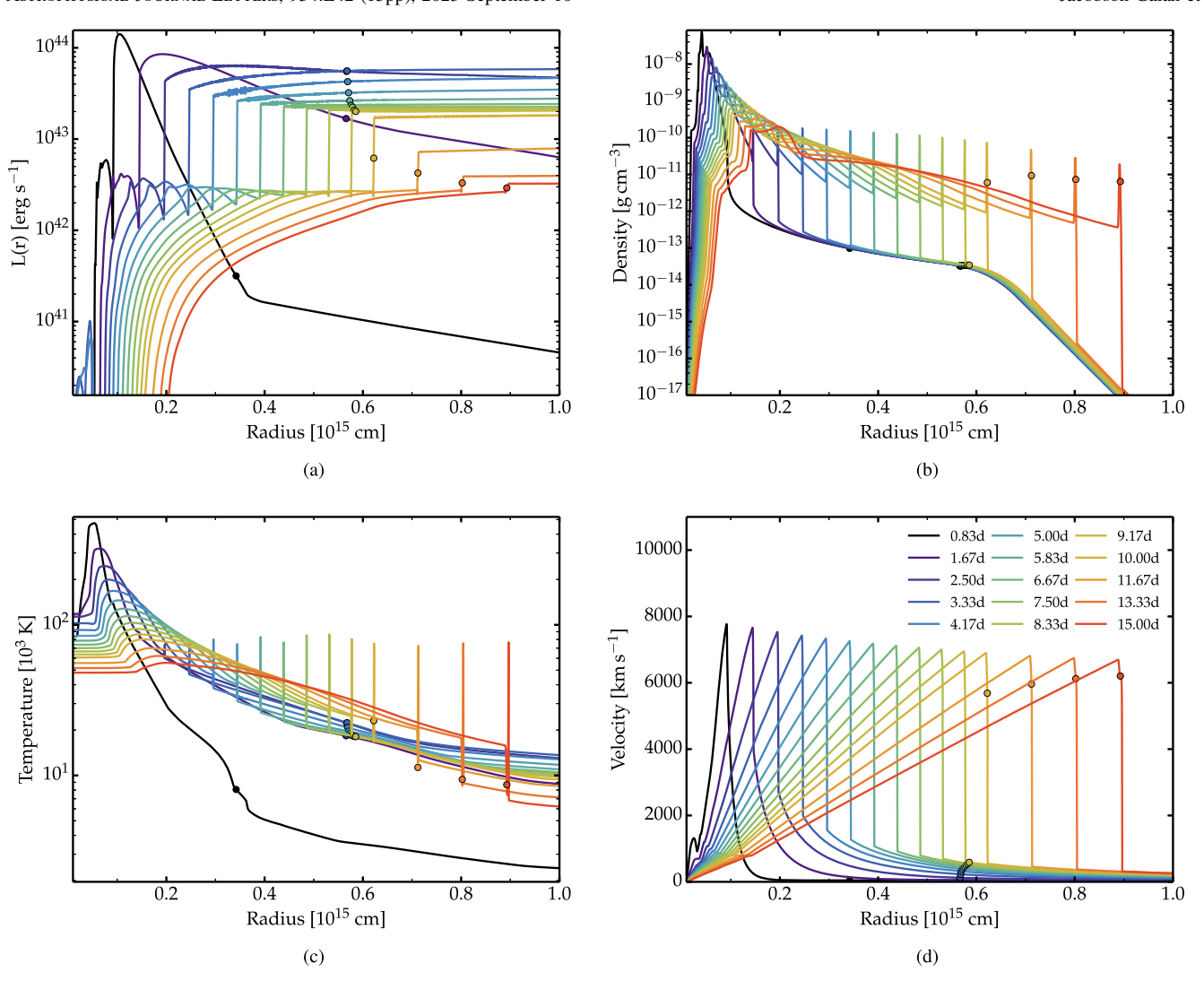


Figure 8. Time series of the (a) luminosity, (b) density, (c) temperature, and (d) velocity vs. radius for best fitting CMFGEN model r1w6b. Circles show the location of the photosphere, which resides in the slow moving CSM until  $\sim$ 8 days and after which recedes into the fast-moving dense shell. The model phases begin at the onset of the radiation hydrodynamics simulation, which is  $\sim$ 1 hr before the shock crosses the progenitor radius (as given in the progenitor stellar model, i.e., without CSM).

Table A2 Model Properties

Name	$t_{\rm IIn}$ (days)	$(M_{\odot} \text{ yr}^{-1})$	$ ho_{\text{CSM},14}^{\text{PCSM},14}$ (g cm <sup>-3</sup> )	R <sub>CSM</sub> (cm)	Reference
rlw1h	< 0.3	1.0e-06	2.7e-12	$3 \times 10^{14}$	Dessart et al. (2017)
r1w1	< 0.1	1.0e-06	1.0e-16	$1 \times 10^{15}$	Dessart et al. (2017)
r2w1	< 0.2	1.0e-06	9.0e-16	$1 \times 10^{14}$	Dessart et al. (2017)
r1w4	1.4	1.0e-03	1.0e-13	$5 \times 10^{14}$	Dessart et al. (2017)
r1w5h	0.9	3.0e-03	5.0e-13	$3 \times 10^{14}$	Dessart et al. (2017)
r1w5r	1.4	5.0e-03	5.0e-13	$4 \times 10^{14}$	Dessart et al. (2017)
r1w6	3.5	1.0e-02	1.0e-12	$5 \times 10^{14}$	Dessart et al. (2017)
r1w6a	5.5	1.0e-02	1.0e-12	$6 \times 10^{14}$	This work
r1w6b	7.0	1.0e-02	1.0e-12	$8 \times 10^{14}$	This work
r1w6c	9.0	1.0e-02	1.0e-12	$1 \times 10^{15}$	Jacobson-Galán et al. (2022)
r1w7a	14.0	3.0e-02	3.0e-12	$1 \times 10^{15}$	Jacobson-Galán et al. (2022)
r1w7b	25.0	3.0e-02	3.0e-12	$2 \times 10^{15}$	Jacobson-Galán et al. (2022)
r1w7c	35.0	3.0e-02	3.0e-12	$4 \times 10^{15}$	Jacobson-Galán et al. (2022)
r1w7d	35.0	3.0e-02	3.0e-12	$8 \times 10^{15}$	Jacobson-Galán et al. (2022)
m1em5	< 0.1	1.0e-05	6.1e-16	$1 \times 10^{16}$	Dessart & Jacobson-Galán (2023)
m1em4	< 0.2	1.0e-04	5.2e-15	$1 \times 10^{16}$	Dessart & Jacobson-Galán (2023)
m1em3	1.0	1.0e-03	5.4e-14	$1 \times 10^{16}$	Dessart & Jacobson-Galán (2023)
m1em2	4.0	1.0e-02	1.3e-12	$1 \times 10^{16}$	Dessart & Jacobson-Galán (2023)
m1em1	15.0	1.0e-01	1.4e-11	$1 \times 10^{16}$	Dessart & Jacobson-Galán (2023)
m1em0	25.0	1.0e+00	7.3e-11	$1 \times 10^{16}$	Dessart & Jacobson-Galán (2023)

#### Note.

#### **ORCID iDs**

- W. V. Jacobson-Galán https://orcid.org/0000-0003-1103-3409
- L. Dessart https://orcid.org/0000-0003-0599-8407
- R. Margutti https://orcid.org/0000-0003-4768-7586
- R. Chornock https://orcid.org/0000-0002-7706-5668
- R. J. Foley https://orcid.org/0000-0002-2445-5275
- C. D. Kilpatrick https://orcid.org/0000-0002-5740-7747
- D. O. Jones https://orcid.org/0000-0002-6230-0151
- K. Taggart https://orcid.org/0000-0002-5748-4558
- C. R. Angus https://orcid.org/0000-0002-4269-7999
- S. Bhattacharjee https://orcid.org/0000-0002-7350-7043
- L. A. Braff https://orcid.org/0009-0000-2983-1017
- D. Brethauer https://orcid.org/0000-0001-6415-0903
- A. J. Burgasser https://orcid.org/0000-0002-6523-9536
- K. C. Chambers https://orcid.org/0000-0001-6965-7789
- D. A. Coulter https://orcid.org/0000-0003-4263-2228
- E. Dominguez-Ruiz https://orcid.org/0009-0009-5524-8525
- C. B. Dickinson https://orcid.org/0000-0001-9749-4200
- T. de Boer https://orcid.org/0000-0001-5486-2747
- A. Gagliano https://orcid.org/0000-0003-4906-8447
- C. Gall https://orcid.org/0000-0002-8526-3963
- H. Gao https://orcid.org/0000-0003-1015-5367
- E. L. Gates https://orcid.org/0000-0002-3739-0423
- S. Gomez https://orcid.org/0000-0001-6395-6702
- M. Guolo https://orcid.org/0000-0002-0786-7307
- M. R. J. Halford https://orcid.org/0000-0002-5440-2350
- J. Hjorth https://orcid.org/0000-0002-4571-2306
- M. E. Huber https://orcid.org/0000-0003-1059-9603
- M. N. Johnson https://orcid.org/0009-0008-2688-0815
- T. Laskar https://orcid.org/0000-0003-1792-2338
- N LeBaron https://orcid.org/0000-0002-2249-0595
- Z. Li https://orcid.org/0000-0002-4860-7667
- S. D. Loch https://orcid.org/0000-0002-3822-6756
- E. A. Magnier https://orcid.org/0000-0002-7965-2815

- D. J. Matthews https://orcid.org/0000-0002-4513-3849
- H.-Y. Miao https://orcid.org/0000-0003-2736-5977
- D. Milisavljevic https://orcid.org/0000-0002-0763-3885
- Y.-C. Pan https://orcid.org/0000-0001-8415-6720
- C. L. Ransome https://orcid.org/0000-0003-4175-4960
- J. M. Rees https://orcid.org/0000-0002-5376-3883
- A. Rest https://orcid.org/0000-0002-4410-5387
- C. Rojas-Bravo https://orcid.org/0000-0002-7559-315X
- N. R. Sandford https://orcid.org/0000-0002-7393-3595
- L. Sandoval Ascencio https://orcid.org/0000-0001-8568-8729
- A. Savino https://orcid.org/0000-0002-1445-4877
- H. Sears https://orcid.org/0000-0001-8023-4912
- S. J. Smartt https://orcid.org/0000-0002-8229-1731
- E. R. Softich https://orcid.org/0000-0002-1420-1837
- C. A. Theissen https://orcid.org/0000-0002-9807-5435
- S. Tinyanont https://orcid.org/0000-0002-1481-4676
- V. A. Villar https://orcid.org/0000-0002-5814-4061
- Q. Wang https://orcid.org/0000-0001-5233-6989
- R. J. Wainscoat https://orcid.org/0000-0002-1341-0952
- A. L. Westerling https://orcid.org/0009-0003-8229-0127
- M. A. Wozniak https://orcid.org/0000-0002-1033-3656
- S. K. Yadavalli https://orcid.org/0000-0002-0840-6940
- Y. Zenati https://orcid.org/0000-0002-0632-8897

Anderson, J. P., González-Gaitán, S., Hamuy, M., et al. 2014, ApJ, 786, 67 Beasor, E. R., Davies, B., Smith, N., et al. 2020, MNRAS, 492, 5994 Becker, A. 2015, HOTPANTS: High Order Transform of PSF ANd Template Subtraction, Astrophysics Source Code Library, ascl:1504.004

References

Berger, E., Keating, G., Alexander, K., et al. 2023, TNSAN, 131, 1 Boian, I., & Groh, J. H. 2020, MNRAS, 496, 1325

Bruch, R. J., Gal-Yam, A., Schulze, S., et al. 2021, ApJ, 912, 46 Bruch, R. J., Gal-Yam, A., Yaron, O., et al. 2023, ApJ, 952, 23

Chambers, K. C., Huber, M. E., Flewelling, H., et al. 2017, TNSTR, 2017-324, 1

<sup>&</sup>lt;sup>a</sup> Density at 10<sup>14</sup> cm.

```
Chandra, P., Chevalier, R., Nayana, A. J., Maeda, K., & Ray, A. 2023, ATel,
   16052, 1
Chugai, N. N. 2001, MNRAS, 326, 1448
Coulter, D. A., Jones, D. O., McGill, P., et al. 2022, YSE-PZ: An Open-source
  Target and Observation Management System, v0.3.0, Zenodo, doi:10.5281/
   zenodo.7278430
Coulter, D. A., Jones, D. O., McGill, P., et al. 2023, PASP, 135, 064501
Davies, B., & Dessart, L. 2019, MNRAS, 483, 887
Davies, B., Plez, B., & Petrault, M. 2022, MNRAS, 517, 1483
Davis, K. W., Taggart, K., Tinyanont, S., et al. 2023, MNRAS, 523, 2530
Dessart, L., Audit, E., & Hillier, D. J. 2015, MNRAS, 449, 4304
Dessart, L., & Hillier, D. J. 2022, A&A, 660, L9
Dessart, L., Hillier, D. J., Audit, E., Livne, E., & Waldman, R. 2016, MNRAS,
Dessart, L., Hillier, D. J., Gezari, S., Basa, S., & Matheson, T. 2009, MNRAS,
   394, 21
Dessart, L., Hillier, D. J., Waldman, R., & Livne, E. 2013, MNRAS, 433, 1745
Dessart, L., & Jacobson-Galán, W. V. 2023, A&A, N/A, N/A
Dessart, L., John Hillier, D., & Audit, E. 2017, A&A, 605, A83
Fassia, A., Meikle, W. P. S., Chugai, N., et al. 2001, MNRAS, 325, 907
Finkbeiner, D. P., Schlafly, E. F., Schlegel, D. J., et al. 2016, ApJ, 822, 66
Fitzpatrick, E. L. 1999, PASP, 111, 63
Flewelling, H. A., Magnier, E. A., Chambers, K. C., et al. 2020, ApJS, 251, 7
Fuller, J. 2017, MNRAS, 470, 1642
Gaia Collaboration 2022, yCat, I/355
Gal-Yam, A., Arcavi, I., Ofek, E. O., et al. 2014, Natur, 509, 471
González, M., Audit, E., & Huynh, P. 2007, A&A, 464, 429
Grefenstette, B. W., Brightman, M., Earnshaw, H. P., Harrison, F. A., &
   Margutti, R. 2023, ApJL, 952, L3
Groh, J. H. 2014, A&A, 572, L11
Hillier, D. J., & Dessart, L. 2012, MNRAS, 424, 252
Hiramatsu, D., Howell, D. A., Van Dyk, S. D., et al. 2021, NatAs, 5, 903
Horne, K. 1986, PASP, 98, 609
Huang, C., & Chevalier, R. A. 2018, MNRAS, 475, 1261
Itagaki, K. 2023, TNSTR, 2023-1158, 1
Jacobson-Galán, W. V., Dessart, L., Jones, D. O., et al. 2022, ApJ, 924, 15
Jacobson-Galán, W. V., Margutti, R., Kilpatrick, C. D., et al. 2020, ApJ,
Jones, D. O., Foley, R. J., Narayan, G., et al. 2021, ApJ, 908, 143
Kaiser, N., Aussel, H., Burke, B. E., et al. 2002, Proc. SPIE, 4836, 154
Khazov, D., Yaron, O., Gal-Yam, A., et al. 2016, ApJ, 818, 3
Kilpatrick, C. D., Foley, R. J., Jacobson-Galán, W. V., et al. 2023, ApJL,
   952. 11
Kilpatrick, C. D., Takaro, T., Foley, R. J., et al. 2018, MNRAS, 480, 2072
Leonard, D. C., Filippenko, A. V., Barth, A. J., & Matheson, T. 2000, ApJ,
Lundquist, M., O'Meara, J., & Walawender, J. 2023, TNSAN, 160, 1
```

```
Magnier, E. A., Schlafly, E. F., Finkbeiner, D. P., et al. 2020, ApJS, 251, 6
Mao, Y., Zhang, M., Cai, G., et al. 2023, TNSAN, 130, 1
Martini, P., Elias, J., Points, S., et al. 2014, Proc. SPIE, 9147, 91470Z
Matthews, D., Margutti, R., Alexander, K. D., et al. 2023, TNSAN, 146, 1
McCully, C., Volgenau, N. H., Harbeck, D.-R., et al. 2018, Proc. SPIE, 10707,
Miller, J. S., & Stone, R. P. S. 1993, The Kast Double Spectograph, Lick
  Observatory Technical Reports 66, Univ. of California, https://mthamilton.
  ucolick.org/techdocs/instruments/kast/Tech%20Report%2066%20KAST%
  20Miller%20Stone.pdf
Owocki, S. P., Gayley, K. G., & Shaviv, N. J. 2004, ApJ, 616, 525
Owocki, S. P., Townsend, R. H. D., & Quataert, E. 2017, MNRAS, 472, 3749
Pan, Y. C., Foley, R. J., Jones, D. O., Filippenko, A. V., & Kuin, N. P. M.
   2020, MNRAS, 491, 5897
Perley, D. A., Gal-Yam, A., Irani, I., & Zimmerman, E. 2023, TNSAN, 119, 1
Poznanski, D., Prochaska, J. X., & Bloom, J. S. 2012, MNRAS, 426, 1465
Quataert, E., Fernández, R., Kasen, D., Klion, H., & Paxton, B. 2016,
          S, 458, 1214
Quataert, E., & Shiode, J. 2012, MNRAS, 423, L92
Rest, A., Stubbs, C., Becker, A. C., et al. 2005, ApJ, 634, 1103
Riess, A. G., Macri, L. M., Hoffmann, S. L., et al. 2016, ApJ, 826, 56
Riess, A. G., Yuan, W., Macri, L. M., et al. 2022, ApJL, 934, L7
Schechter, P. L., Mateo, M., & Saha, A. 1993, PASP, 105, 1342
Schlafly, E. F., & Finkbeiner, D. P. 2011, ApJ, 737, 103
Schlegel, D. J., Finkbeiner, D. P., & Davis, M. 1998, ApJ, 500, 525
Shivvers, I., Groh, J. H., Mauerhan, J. C., et al. 2015, ApJ, 806, 213
Smith, N. 2014, ARA&A, 52, 487
Smith, N., Mauerhan, J. C., Cenko, S. B., et al. 2015, MNRAS, 449, 1876
Stritzinger, M., Valerin, G., Elias-Rosa, N., et al. 2023, TNSAN, 145, 1
Tartaglia, L., Sand, D. J., Groh, J. H., et al. 2021, ApJ, 907, 52
Teja, R. S., Singh, A., Sahu, D. K., et al. 2022, ApJ, 930, 34
Tody, D. 1986, Proc. SPIE, 627, 733
Tody, D. 1993, in ASP Conf. Ser. 52, Astronomical Data Analysis Software
  and Systems II, ed. R. J. Hanisch, J. V. Brissenden, & J. Barnes (San
  Francisco, CA: ASP), 173
Terreran, G., Jacobson-Galán, W. V., Groh, J. H., et al. 2022, ApJ, 926, 20
Terreran, G., Jerkstrand, A., Benetti, S., et al. 2016, MNRAS, 462, 137
Tinyanont, S., Ridden-Harper, R., Foley, R. J., et al. 2022, MNRAS, 512, 2777
Tsuna, D., Murase, K., & Moriya, T. J. 2023, ApJ, 952, 11
Vaytet, N. M. H., Audit, E., Dubroca, B., & Delahaye, F. 2011, JQSRT,
  112, 1323
Wang, Q., Goel, A., Dessart, L., et al. 2023, arXiv:2305.05015
Waters, C. Z., Magnier, E. A., Price, P. A., et al. 2020, ApJS, 251, 4
Wu, S., & Fuller, J. 2021, ApJ, 906, 3
Yamanaka, M., Fujii, M., & Nagayama, T. 2023, PASJ, N/A, N/A
Yaron, O., Perley, D. A., Gal-Yam, A., et al. 2017, NatPh, 13, 510
Zhang, J., Wang, X., József, V., et al. 2020, MNRAS, 498, 84
```